Systematic Investigation of Anisotropic Magneto–Peltier Effect and Anomalous Ettingshausen Effect in Ni Thin Films

Raja Das,[1,†,‡] Ryo Iguchi,[1] and Ken-ichi Uchida[1,2,3,*]

[1]*National Institute for Materials Science, Tsukuba 305-0047, Japan*
[2]*Center for Spintronics Research Network, Tohoku University, Sendai 980-8577, Japan*
[3]*Department of Mechanical Engineering, The University of Tokyo, Tokyo 113-8656, Japan*

The anisotropic magneto–Peltier effect (AMPE) and the anomalous Ettingshausen effect (AEE) are investigated in U-shaped Ni thin films of differing thickness and substrate by means of the lock-in-thermography (LIT) method. We establish a procedure to extract pure AMPE and AEE contributions, separated from other thermoelectric effects, for ferromagnetic thin films. The measurements of the magnetic-field-angle θ_H dependence of the LIT images clearly show that the temperature modulation induced by the AMPE (AEE) in the Ni films varies with a $\cos 2\theta_H$ ($\cos \theta_H$) pattern, confirming the symmetry of the AMPE (AEE). The systematic LIT measurements with various substrates show that the AMPE-induced temperature modulation decreases with the increase in thermal conductivity of the substrates, whereas the AEE-induced temperature modulation is almost independent of the thermal conductivity, indicating that the heat loss into the substrates plays an important role in determining the magnitude of the AMPE-induced temperature modulation in thin films. Our experimental results are reproduced by numerical calculations based on a two-dimensional finite-element method. These findings provide a platform for investigating the AMPE and AEE in thin-film devices.

I. INTRODUCTION

The Seebeck and Peltier effects are the fundamental thermoelectric phenomena in electric conductors [1,2]. The Seebeck effect, which was discovered by Thomas Johann Seebeck in 1821, refers to the conversion of a heat current into a charge current, enabling thermoelectric voltage generation from waste heat. The Peltier effect, which was discovered by Jean Charles Athanase Peltier in 1834, is the Onsager reciprocal of the Seebeck effect. This phenomenon refers to the conversion of a charge current into a heat current, and generates a temperature increase and decrease at the junction of two conductors due to the difference in their Peltier coefficients. Since the Peltier effect enables direct electrical cooling or heating, it is used in solid-state heat pumps and temperature controllers. In these fundamental thermoelectric conversion phenomena, the charge and heat currents flow parallel to each other.

In magnetic materials, in addition to the Seebeck and Peltier effects, a variety of thermoelectric and thermo-spin effects are induced by the concerted action of spin-polarized electron transport and spin-orbit interaction [3–46]. Some of these thermoelectric conversion phenomena, such as the anisotropic magneto–Seebeck effect [5, 12,22,26–29,37] and the anomalous Nernst effect [9,10,13, 42], were discovered many decades ago, but the physics and materials science have not been developed sufficiently. This situation is changing with rapid developments of spin caloritronics [24,32], where these phenomena are attracting renewed attention. In this line, the observation of the anisotropic magneto–Peltier effect (AMPE) [37,41,45], the reciprocal of the anisotropic magneto–Seebeck effect, and the anomalous Ettingshausen effect (AEE) [39,41–43], the reciprocal of the anomalous Nernst effect, in ferromagnetic metals was recently reported.

The AMPE is a phenomenon that the Peltier coefficient depends on the angle θ_M between the directions of the charge current $\mathbf{J}_c$ and magnetization $\mathbf{M}$ in a ferromagnet. Because of the AMPE, the Peltier coefficient Π in an isotropic ferromagnet exhibits θ_M dependence satisfying the following equation:

$$\Pi(\theta_M) = \Pi_\perp + \left(\Pi_{||} - \Pi_\perp \right) \cos^2 \theta_M, \qquad (1)$$

*uchida.kenichi@nims.go.jp

†Present address: Faculty of Materials Science and Engineering, Phenikaa Institute for Advanced Study, Phenikaa University, Hanoi 10000, Vietnam

‡Present address: Phenikaa Research and Technology Institute, A&A Green Phoenix Group, Hanoi 10000, Vietnam

where $\Pi_{\parallel(\perp)}$ is the Peltier coefficient for the $\mathbf{M} \parallel \mathbf{J}_c$ ($\mathbf{M} \perp \mathbf{J}_c$) configuration. This symmetry is similar to that of the anisotropic magnetoresistance in an isotropic ferromagnet [6]. If the finite AMPE appears, by the formation of a nonuniform magnetization configuration, Peltier cooling and heating can be generated between the areas with different θ_M values even in the absence of junction structures, and the magnitude of the resultant temperature change is proportional to $\Pi_{\parallel} - \Pi_{\perp}$. In 2018, the temperature change induced by the AMPE was directly observed in a polycrystalline Ni slab with a U-shaped structure [41], where the Ni slab was uniformly magnetized and a charge current was applied along the U-shaped structure. This configuration allows us to realize the nonuniform θ_M distribution; the AMPE-induced temperature modulation appears around the corners of the U-shaped structure; that is, the region between the area satisfying $\mathbf{M} \perp \mathbf{J}_c$ and the area satisfying $\mathbf{M} \parallel \mathbf{J}_c$ [Fig. 1(a)]. The AMPE has been observed not only in Ni but also in several ferromagnetic metals, such as $Ni_{95}Pt_5$ and $Ni_{95}Pd_5$ [41]. Importantly, the magnitude of the AMPE signal for $Ni_{95}Pt_5$ was found to be much greater than that for Ni, showing the important role of spin-orbit interaction in the AMPE [41]. Since the thermoelectric properties of the AMPE can be redesigned simply by changing the shape of ferromagnets or magnetization configurations, it provides new concepts in thermal-management technologies for electronic and spintronic devices. Owing to the absence of a junction structure, AMPE-based devices can be easily integrated in nanoscale devices and circuits where conventional thermoelectric devices cannot be integrated due to the complicated structure.

In a ferromagnet, the transverse thermoelectric effect called the "anomalous Ettingshausen effect" also appears. The AEE generates a heat current in the direction of the cross product of $\mathbf{J}_c$ and $\mathbf{M}$:

$$\mathbf{j}_{q,\text{AEE}} = \Pi_{\text{AEE}}(\mathbf{j}_c \times \hat{\mathbf{m}}), \tag{2}$$

where $\mathbf{j}_{q,\text{AEE}}$, $\mathbf{j}_c$, $\hat{\mathbf{m}}$, and Π_{AEE} denote the heat-current density driven by the AEE, the charge-current density applied to a ferromagnet, the unit vector of $\mathbf{M}$, and the anomalous Ettingshausen coefficient, respectively [Fig. 1(a)] [39, 41–43]. Therefore, when Π_{AEE} is isotropic in a ferromagnet, the temperature gradient induced by the AEE should be proportional to $\sin \theta_M$. The AEE may also allow the realization of novel thermal-management technologies because it enables magnetic control of a heat-current direction.

The understanding of the microscopic mechanism of the AMPE and the AEE in ferromagnetic conductors and increase of their thermoelectric conversion efficiency are crucial not only for the fundamental physics of spin caloritronics and thermoelectrics but also for the

realization of nanoscale thermal-energy engineering. However, despite their scientific and technological importance, few studies on the AMPE and AEE have been reported so far, and more-comprehensive studies are necessary. Although the direct observation of the AMPE has been reported only for bulk ferromagnetic metal slabs, thin films make it easier to perform systematic measurements, including the measurement of the composition dependence and the effect of alloy ordering [44,45], which accelerates research to find and develop materials exhibiting good thermoelectric conversion properties. Investigation of the AMPE in thin films is important also for integrating it in spintronic and spin-caloritronic devices for their thermal management. Significantly, in thin films formed on substrates, the magnitude of the AMPE-induced temperature modulation should depend not only on the physical properties of the films but also on the film dimensions and thermal properties of the substrates due to heat loss from the films to the substrates [21,30,35]. The role of the substrates in AEE experiments is also yet to be investigated systematically. The purpose of this study is to establish a procedure for the detection of the AMPE and AEE contributions in thin films and to clarify the dependences of the AMPE and AEE on the thickness of the films and thermal properties of the substrates.

In this paper, we report the observation of the AMPE and AEE in Ni thin films with differing film thickness and substrate materials by means of the lock-in-thermography (LIT) method [38–45,47–49]. We demonstrate that the pure AMPE and AEE contributions, separated from other thermoelectric effects, can be extracted even in thin films by measuring the magnetic-field-angle dependence of the LIT images. The field-angle dependence of the AMPE and AEE signals is confirmed to show the symmetries consistent with Eqs. (1) and (2), respectively. We also find that both the AMPE-induced temperature modulation and the AEE-induced temperature modulation increase almost linearly with the increase in the Ni-film thickness and that the AMPE-induced temperature modulation decreases with the increase in thermal conductivity of the substrates, whereas the AEE-induced temperature modulation is nearly independent of the thermal conductivity of the substrates. These detailed studies provide new insights to reveal the parameters that are relevant for optimizing the device geometry and material selection for practical applications of these phenomena and for their basic understanding.

This paper is organized as follows. In Sec. II, we explain the details of the experimental procedures and configurations for the measurements of the AMPE and AEE using the LIT method. In Sec. III, we report the observation of the AMPE- and AEE-induced temperature modulation in Ni films, followed by numerical calculations to explain the observed behaviors. Section IV is devoted to the conclusions.

II. EXPERIMENTAL PROCEDURE

The samples used in this study are U-shaped Ni thin films of various thicknesses (50, 100, 150, and 200 nm) deposited on glass, gadolinium gallium garnet (GGG), and sapphire substrates with a size of $10 \times 10 \times 0.5$ mm^3 by use of an rf magnetron-sputtering system. Immediately before the deposition, the substrates are cleaned with acetone and ethanol with use of an ultrasonic cleaner. The rf power and Ar-gas pressure for the Ni deposition are kept fixed at 50 W and 0.3 Pa, respectively. The deposition rate is 0.019 nm s^{-1} for all the samples. The Ni films are formed on the well-polished 10×10 mm^2 surface of the substrates and patterned into a U-shaped structure by sputtering Ni through a metallic shadow mask, where the width of the area $B_{L/R/C}$ is 0.2 mm [Fig. 1(b)]. The thickness of the deposited films is measured with a stylus surface profilometer. To determine the saturation field of the films, anisotropic magnetoresistance measurements are performed. It is found that the magnetization of the Ni films saturates under an in-plane magnetic field **H** with magnitude of $H > 10$ Oe. In the U-shaped Ni film, when

H is applied along the x direction and **M** is aligned along the **H** direction, the AMPE signal appears around the corner $C_{L/R}$, the region between the area $B_{L/R}$ satisfying **M** $\perp$ $\mathbf{J}_c$ and the area B_C satisfying **M** $||$ $\mathbf{J}_c$, while the AEE signal appears in $B_{L/R}$ [Figs. 1(a) and 1(b)]. Therefore, the AMPE and the AEE can be separated from each other by the position or spatial distribution of temperature-modulation signals. The magnitude of the AMPE and AEE signals increases with increasing $|H|$ following the magnetization curve of the Ni films and becomes constant after the saturation field. Importantly, the AMPE (AEE) signals exhibit even (odd) dependence on the H sign when **M** is along the x direction [Eqs. (1) and (2)] [41]. In this paper, we focus on the bulk thermoelectric conversion properties and ignore interface and surface effects because the thickness of the Ni films used here is much greater than typical electron spin or magnon diffusion lengths.

The measurements of the AMPE and AEE in the Ni films are performed by the LIT method [Fig. 1(c)] [38–45,47–49]. In the LIT experiments, we measure the spatial distribution of infrared radiation thermally emitted from the sample surface with high temperature and spatial
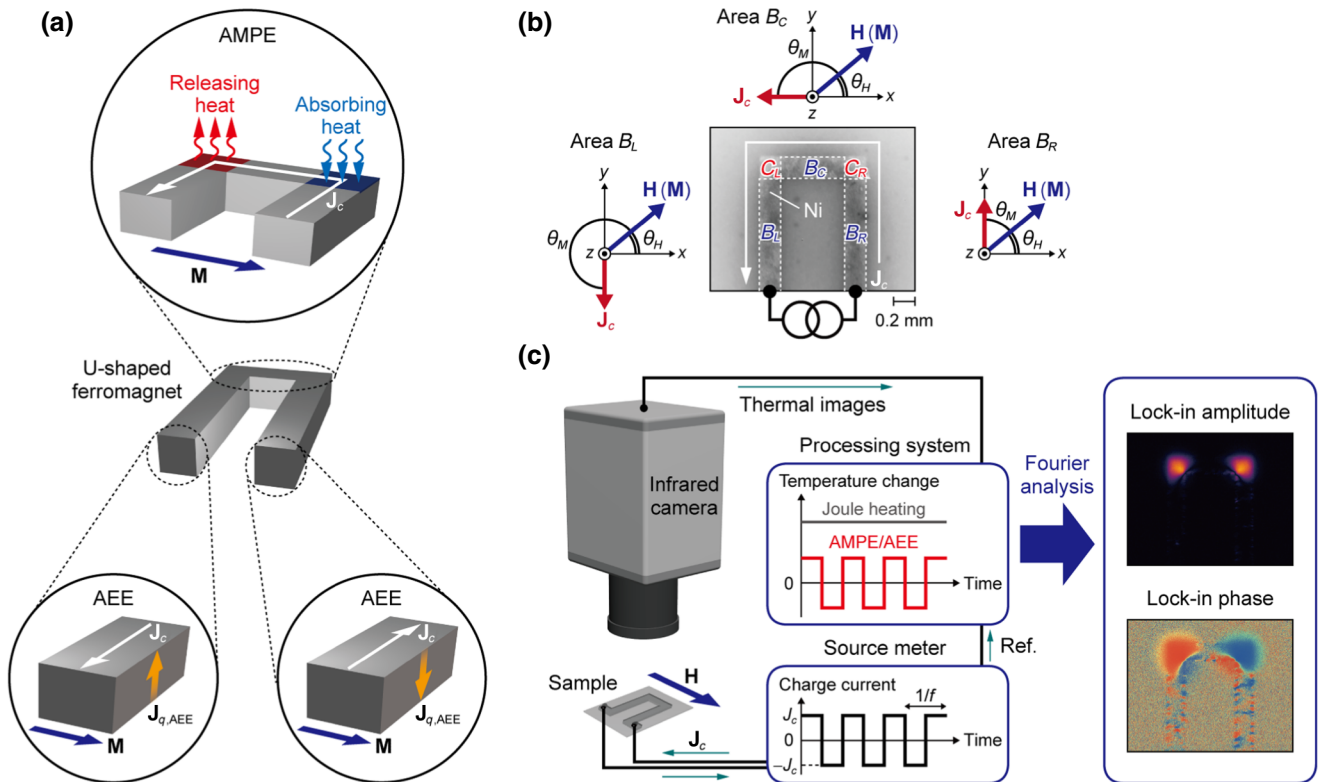

FIG. 1. (a) The U-shaped ferromagnetic metal used for measuring the AMPE and AEE. **M**, $\mathbf{J}_c$, and $\mathbf{J}_{q,\text{AEE}}$ denote the magnetization vector, charge current applied to the ferromagnetic metal (with magnitude J_c), and heat current induced by the AEE. (b) Steady-state infrared image of the U-shaped Ni thin film with black-ink coating and the definitions of θ_M and θ_H. θ_H (θ_M) represents the angle between the magnetic field vector **H** and the $+x$ direction (between $\mathbf{J}_c$ and **M**), where the relations between θ_M and θ_H are defined when **M** is aligned along **H**. The area $B_{L/C/R}$, surrounded by dotted white lines, and the area $C_{L/R}$, the corner of the U-shaped structure, are the relevant parts of the Ni film. (c) LIT method used for the measurements of the AMPE and AEE. f denotes the frequency of the charge current (i.e., the lock-in frequency). All LIT measurements are performed at $|H| = 100$ Oe, where H denotes the magnitude of **H**.

resolution, enabling quantitative measurements of the AMPE- and AEE-induced temperature modulation in the Ni films. To enhance infrared emissivity, the surface of the samples is coated with insulating black ink, for which the emissivity is greater than 0.95. During the LIT measurements, a square-wave-modulated ac charge current with amplitude J_c, frequency f, and zero dc offset is applied to the Ni films and the sample is fixed on an Al block, which can be regarded as a heat bath. The thermal images oscillating with the same frequency as the input charge current are then extracted through Fourier analysis. The contribution of the thermoelectric effects (proportional to J_c) can be separated from the Joule-heating background (proportional to $J_c{}^2$) by extraction of the first-harmonic response of the thermal images, since the Joule heating generated in this condition is constant with time. As a result of the Fourier analysis, the thermal images obtained are transformed into the lock-in amplitude A and phase ϕ images. The A image shows the distribution of the magnitude of the current-induced temperature modulation and the ϕ image shows the distribution of the sign of the temperature modulation in addition to the time delay due to thermal diffusion, where A and ϕ values are defined in the ranges $A \geq 0$ and $0° \leq \phi < 360°$, respectively. The detected infrared radiation is converted into temperature information through the calibration method described in Ref. [41]. The LIT images are measured while **H** with a magnitude of $H = 100$ Oe is applied to the Ni films in the x-y plane at an azimuthal angle θ_H from the $+x$ direction [Fig. 1(b)], where $|H|$ is much greater than the saturation field of the films. All the measurements are performed at room temperature and atmospheric pressure.

The measurements of the magnetic-field-angle θ_H dependence of the temperature modulation enable the pure detection of the AMPE and AEE and the demonstration of their symmetries. To discuss the symmetries of the AMPE and AEE, it is necessary to note the relations between θ_M and θ_H. As shown in Fig. 1(b), the relations are $\theta_M = 270° - \theta_H$, $90° - \theta_H$, and $180° - \theta_H$ in the areas B_L, B_R, and B_C of the U-shaped structure, respectively. Solving the trigonometric relations in Eq. (1) [Eq. (2)], we find that the temperature modulation induced by the AMPE (AEE) in the U-shaped ferromagnet is proportional to $\cos 2\theta_H$ ($\cos\theta_H$). Hereafter, the symmetries of the AMPE and AEE are discussed in terms of θ_H, not θ_M.

III. RESULTS AND DISCUSSION

A. Fundamental measurements and analyses

In Figs. 2(a)–2(d), we show the A and ϕ images for the U-shaped 100-nm-thick Ni film on the glass substrate for $\theta_H = 0°$, $90°$, $180°$, and $270°$, respectively, measured at $f = 25$ Hz and $J_c = 40$ mA. To determine the positions of the AMPE- and AEE-induced heat sources and sinks, the lock-in frequency f is fixed at the maximum value, because

the temperature broadening due to thermal diffusion is reduced by increase of f, where the maximum f value for the frame size used in this study (640×512 pixels) is 25 Hz. A clear charge-current-induced temperature modulation appears in the Ni film at all θ_H values. As discussed above, to separate the AMPE (AEE) contributions, we extract the component showing $\cos 2\theta_H$ ($\cos\theta_H$) symmetry from the raw LIT images, where the LIT amplitude and phase of the $\cos 2\theta_H$ ($\cos\theta_H$) component are denoted by A_{AMPE} (A_{AEE}) and ϕ_{AMPE} (ϕ_{AEE}), respectively. Figure 2(e) shows the A_{AMPE} and ϕ_{AMPE} images for the U-shaped 100-nm-thick Ni film on the glass substrate at $\theta_H = 0°$. We observe clear temperature-modulation signals with $\cos 2\theta_H$ symmetry, which are generated predominantly around $C_{L/R}$ of the U-shaped structure, and the sign of the temperature modulation at C_L is opposite that at C_R because of the ϕ_{AMPE} difference of approximately 180°. This behavior is consistent with the characteristic of the AMPE in ferromagnetic metal slabs [41]. We also confirm that the sign of the temperature modulation at $C_{L/R}$ for the Ni film is the same as that of the AMPE signals for the Ni slab [41]. The detailed behaviors of the AMPE in the Ni film are discussed in Sec. III B, where we show the θ_H dependence of the A_{AMPE} and ϕ_{AMPE} images. In contrast, as shown in the A_{AEE} and ϕ_{AEE} images in Fig. 2(f), the signal with $\cos\theta_H$ symmetry is generated primarily on the area $B_{L/R}$ of the U-shaped structure, where $\mathbf{M} \perp \mathbf{J}_c$. The ϕ_{AEE} difference between B_L and B_R is approximately 180°. The behavior of this temperature modulation is consistent with the characteristic of the AEE in in-plane-magnetized (IM) ferromagnetic metals [39,41–43]. The detailed behaviors of the AEE in the Ni film are discussed in Sec. III C. Here, we also observed background signals in the raw LIT images. In Figs. 2(a)–2(d), in addition to the AMPE and AEE signals, a complicated patchy pattern appears on the whole surface of the Ni film, although no patchy-pattern signals were observed in previous measurements using Ni slabs [41]. The appearance of the patchy pattern could be due to the polycrystalline nature of the thin films, where the Peltier coefficient may have a different value depending on the quality and orientation of the grains. However, since such background coming from the conventional Peltier effect is independent of the magnetic field, it is eliminated in the AMPE and AEE images shown in Figs. 2(e) and 2(f) [see also the H-independent background images shown in Fig. 2(g)]. This procedure of extracting the pure AMPE and AEE signals can be extended to other systems where a complicated temperature modulation is generated due to the polycrystalline nature of the sample.

B. Anisotropic magneto–Peltier effect

We report systematic measurements of the AMPE-induced temperature modulation in the Ni films. Figures 3(a) and 3(b) show the θ_H dependence of the
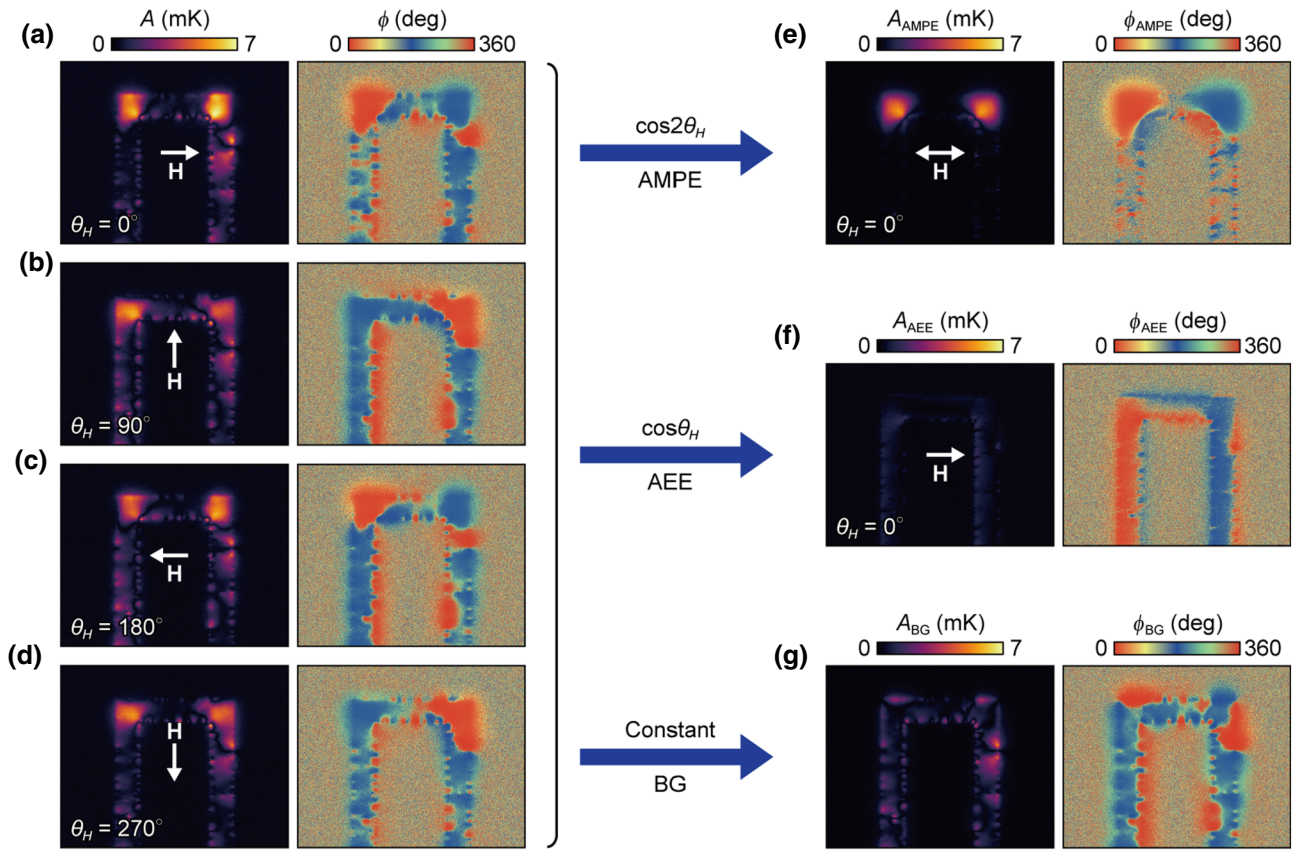
FIG. 2. (a)–(d) Lock-in amplitude A and phase ϕ images for the U-shaped 100-nm-thick Ni film on the glass substrate at $\theta_H = 0°$, 90°, 180°, and 270°, measured at $J_c = 40$ mA and $f = 25$ Hz. (e) A_{AMPE} and ϕ_{AMPE} images for the U-shaped 100-nm-thick Ni film on the glass substrate at $\theta_H = 0°$, $J_c = 40$ mA, and $f = 25$ Hz. (f) A_{AEE} and ϕ_{AEE} images for the U-shaped 100-nm-thick Ni film on the glass substrate at $\theta_H = 0°$, $J_c = 40$ mA, and $f = 25$ Hz. The LIT amplitude and phase with $\cos2\theta_H$ ($\cos\theta_H$) symmetry are denoted by A_{AMPE} (A_{AEE}) and ϕ_{AMPE} (ϕ_{AEE}), respectively. (g) A_{BG} and ϕ_{BG} images for the U-shaped 100-nm-thick Ni film on the glass substrate at $J_c = 40$ mA and $f = 25$ Hz. A_{BG} (ϕ_{BG}) denotes the amplitude (phase) of the temperature modulation due to the H-independent background.

A_{AMPE} and ϕ_{AMPE} images, respectively, for the 100-nm-thick Ni film on the glass substrate at $f = 25$ Hz and $J_c = 40$ mA. The AMPE signal at $C_{L/R}$ at $\theta_H = 90°$ is opposite in sign to that at $\theta_H = 0°$ and the signal disappears at $\theta_H = 45°$, where the disappearance of the AMPE-induced temperature modulation at $C_{L/R}$ is expected as both $B_{L/R}$ and B_C have the same Peltier coefficient at $\theta_H = 45°$ [41]. Figure 3(e) shows ΔT_{AMPE} on C_L and C_R at $f = 25$ Hz and $J_c = 40$ mA as a function of θ_H, where $\Delta T_{\mathrm{AMPE}} = A_{\mathrm{AMPE}}\cos\phi_{\mathrm{AMPE}}$ represents the temperature modulation with sign information if the phase delay due to thermal diffusion is negligibly small. The ΔT_{AMPE} signal varies with θ_H in a $\cos2\theta_H$ pattern at both C_L and C_R and its sign reverses between C_L and C_R for each θ_H value. As discussed in Sec. II, this θ_H dependence of the temperature modulation is consistent with Eq. (1), confirming the symmetry of the AMPE. The behavior of the transverse response of the AMPE (i.e., the planar Ettingshausen effect) for the Ni films is also consistent with that

for the Ni slab and previous expectations [41]; the magnitude of the temperature gradient along the x (y) direction in $B_{L/R}$ (B_C) becomes minimum (maximum) at $\theta_H = 0°$ and 90° ($\theta_H = 45°$). The f dependence of the AMPE-induced temperature modulation for the Ni films is similar to that for the Ni slabs without substrates [41]; the magnitude of A_{AMPE} at C_L and C_R gradually increases with decreasing f, with accompanying temperature broadening due to thermal diffusion [Figs. 3(c), 3(d), 3(f), and 3(g)]. All the experimental results shown in Fig. 3 conclude that the AMPE-induced temperature modulation is detectable even in thin-film ferromagnets formed on substrates.

To understand the effect of the thermal properties of the substrates on the AMPE-induced temperature modulation, we perform LIT measurements using Ni thin films on different substrates. Figures 4(a)–4(c) show the A_{AMPE} and ϕ_{AMPE} images for the U-shaped 100-nm-thick Ni film on the glass, GGG, and sapphire substrates at $f = 25$ Hz and $J_c = 40$, 60, and 75 mA, respectively. Although all the
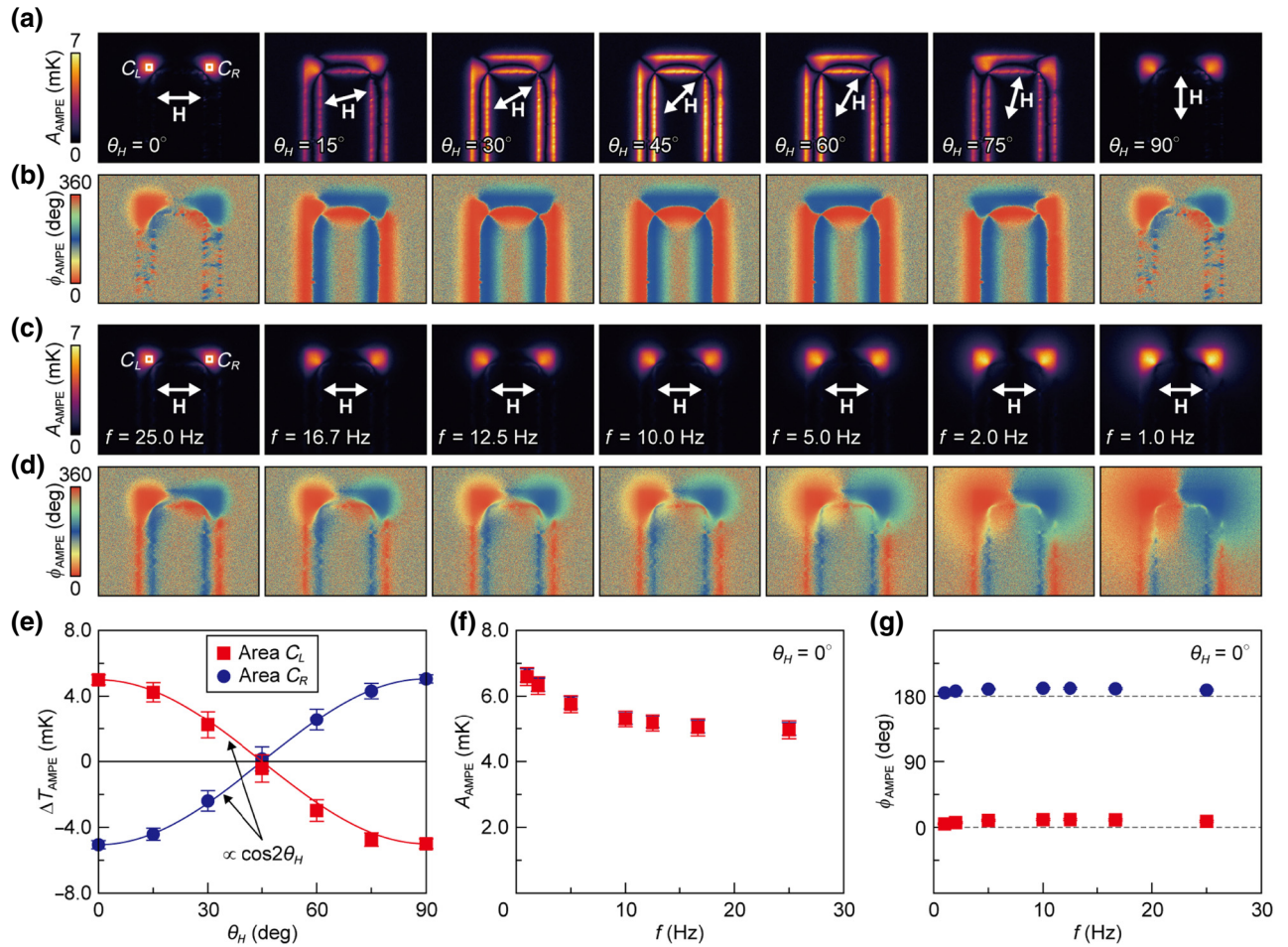
FIG. 3. (a),(b) A_{AMPE} and ϕ_{AMPE} images for the U-shaped 100-nm-thick Ni film on the glass substrate for various values of θ_H, measured at $J_c = 40$ mA and $f = 25$ Hz. (c),(d) A_{AMPE} and ϕ_{AMPE} images for the U-shaped 100-nm-thick Ni film on the glass substrate for various values of f, measured at $\theta_H = 0°$ and $J_c = 40$ mA. (e) θ_H dependence of ΔT_{AMPE} on the area $C_{L/R}$ for the U-shaped 100-nm-thick Ni film on the glass substrate at $J_c = 40$ mA and $f = 25$ Hz. The solid curves show the $\cos 2\theta_H$ functions for comparison with the experimental results. (f),(g) f dependence of A_{AMPE} and ϕ_{AMPE} on $C_{L/R}$ for the U-shaped 100-nm-thick Ni film on the glass substrate, measured at $\theta_H = 0°$ and $J_c = 40$ mA. The data points in (e)–(g) are obtained by our averaging the A_{AMPE} and ϕ_{AMPE} values on $C_{L/R}$ defined by the squares in (a),(c). The error bars represent the standard deviation of the data in the corresponding squares.

samples exhibit clear AMPE-induced temperature modulation, its magnitude in the Ni films on the GGG and sapphire substrates is much smaller than that on the glass substrate. The magnitude of the AMPE signals monotonically decreases with increasing thermal conductivity of the substrates κ_{sub} [see the κ_{sub} dependence of A_{AMPE}/j_c at C_L of the Ni thin films in Fig. 4(h), where j_c represents the charge-current density applied to the Ni films, and the κ_{sub} values are listed in Table I]. As shown in Figs. 4(d)–4(g), the f dependence of the AMPE-induced temperature modulation for the thin films becomes weaker with increasing κ_{sub}. These behaviors are attributed to the heat loss from the Ni films to the substrates, which increases with increasing κ_{sub} in this measurement condition, indicating that the magnitude of the AMPE-induced temperature modulation in thin films is determined by the ratio between the

amount of heat sources and sinks generated by the AMPE and the heat loss to the surroundings. We confirm that the magnitude of the AMPE signals per unit charge-current density increases almost linearly with increasing thickness of the Ni films for all the substrate species [Fig. 4(i)]. These results are reproduced by the numerical calculations described in Sec. III D. Our findings conclude that the magnitude of the AMPE-induced temperature modulation in thin-film devices is determined not only by the thermoelectric properties of the films but also by the film dimensions and thermal boundary conditions and that substrates with lower thermal conductivity are better for obtaining larger AMPE signals in thin films. Importantly, the direct observation of the AMPE in thin films makes it possible to investigate the AMPE in various materials and conditions, because one can obtain information on the
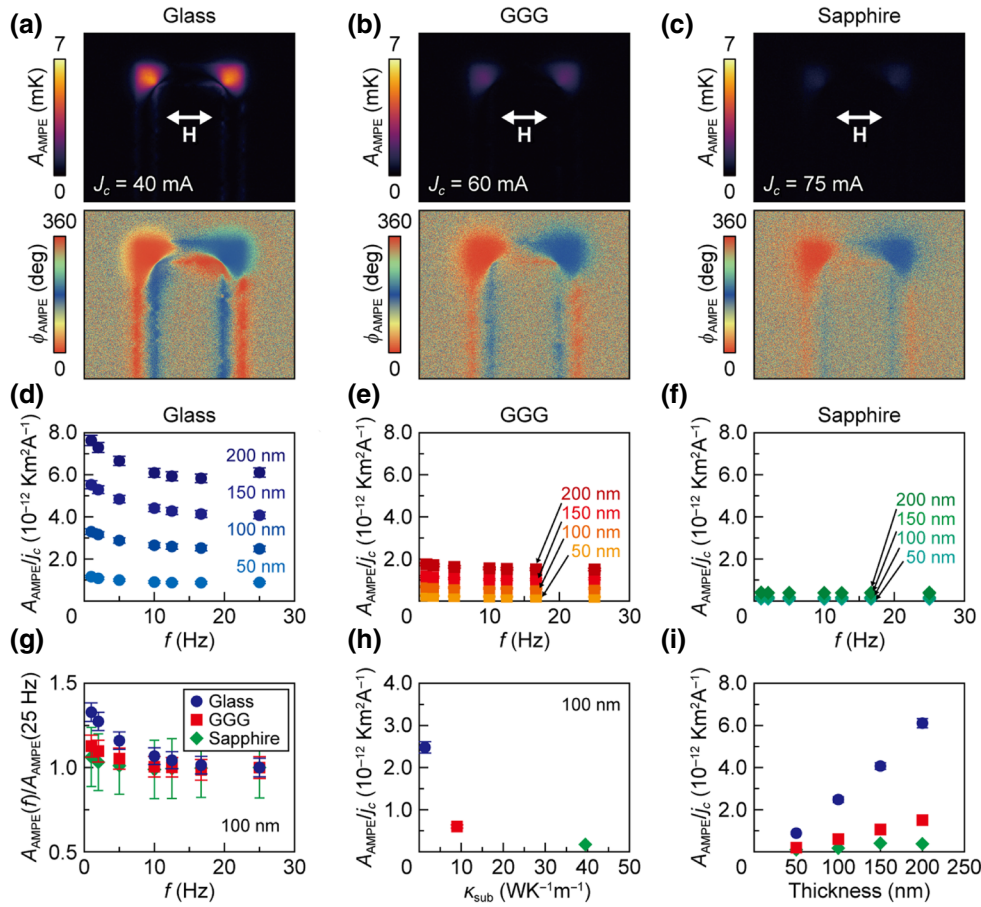
FIG. 4. (a)–(c) A_{AMPE} and ϕ_{AMPE} images for the U-shaped 100-nm-thick Ni film on the glass, GGG, and sapphire substrates, measured at $f = 25$ Hz and $J_c = 40$, 60, and 75 mA, respectively. (d)–(f) f dependence of A_{AMPE}/j_c on C_L for Ni films with various thicknesses on the glass, GGG, and sapphire substrates. j_c represents the charge-current density applied to the Ni films. (g) f dependence of $A_{\text{AMPE}}(f)/A_{\text{AMPE}}(25 \text{ Hz})$ for the U-shaped 100-nm-thick Ni film on the glass, GGG, and sapphire substrates. (h) κ_{sub} dependence of A_{AMPE}/j_c on C_L for the 100-nm-thick Ni films on the glass, GGG, and sapphire substrates at $f = 25$ Hz. κ_{sub} represents the thermal conductivity of the substrates. (i) Ni-film thickness dependence of A_{AMPE}/j_c on C_L for the Ni films on the glass, GGG, and sapphire substrates at $f = 25$ Hz. The error bars represent the standard deviation of the data in the corresponding squares. All the data shown are measured at $\theta_H = 0°$.

sign and relative magnitude of the anisotropy of the Peltier coefficient even from thin film samples as long as the same substrate is used.

C. Anomalous Ettingshausen effect

We are now in a position to investigate the AEE in thin films and clarify its behaviors. To confirm the symmetry of the AEE signal, we systematically explore the θ_H dependence of the AEE-induced temperature modulation. Figures 5(a) and 5(b) show the A_{AEE} and ϕ_{AEE} images, respectively, for various values of θ_H for the 100-nm-thick Ni film on the sapphire substrate at $f = 25$ Hz and $J_c = 75$ mA. The AEE signal in $B_{L/R}$ decreases with increasing θ_H and disappears when $\theta_H = 90°$. The AEE signal in B_C follows the opposite trend to that in $B_{L/R}$; it becomes minimum (maximum) at $\theta_H = 0°$

($\theta_H = 90°$). Figure 5(e) shows ΔT_{AEE} in B_L and B_R at $f = 25$ Hz and $J_c = 75$ mA as a function of θ_H, where $\Delta T_{\text{AEE}} = A_{\text{AEE}}\cos\phi_{\text{AEE}}$. The ΔT_{AEE} signal varies with θ_H in a $\cos\theta_H$ pattern [Fig. 5(e)] in both B_L and B_R and its sign reverses between B_L and B_R for each θ_H value. As discussed in Sec. II, this θ_H dependence of the temperature modulation is consistent with Eq. (2) (recall the relations $\theta_M = 270° - \theta_H$, $90° - \theta_H$, and $180° - \theta_H$ for B_L, B_R, and B_C, respectively). In the A_{AEE} and ϕ_{AEE} images, the contribution coming from the ordinary Ettingshausen effect is negligibly small because of the small magnitude of the external magnetic field [41]. The f dependence of the A_{AEE} and ϕ_{AEE} images is also consistent with the recently observed behavior of the AEE in IM ferromagnetic metal films [39,41–43]; unlike the AMPE signal, the AEE signal in $B_{L/R}$ remains almost constant with f and does not show any temperature broadening from the

TABLE I. Material parameters for numerical calculations.

	Ni	Glass	GGG	Sapphire
Thermal conductivity (W K^{-1} m^{-1}) [56–58]	26	1.4	9.0	39.5
Density (g cm^{-3})	8.9	2.2	7.1	4.0
Specific heat (J g^{-1} K^{-1})	0.44	0.76	0.38	0.76

areas [Figs. 5(c), 5(d), 5(f), and 5(g)]. This result shows that the AEE-induced temperature modulation immediately reaches a steady state, a behavior similar to that of the spin Peltier effect, where the spin-current-induced temperature modulation immediately reaches a steady state due to the presence of dipolar heat sources [38]. The difference in the f dependence between the AMPE and the AEE arises from the aspect ratio of the samples. The AEE induces a heat current along the thickness direction of the Ni films,

while the AMPE induces a heat current along the lateral directions. Since the thickness of the Ni films is 3 orders of magnitude smaller than the lateral size, the AEE-induced temperature change reaches the steady state much faster than the AMPE-induced temperature change, resulting in the constant f dependence of the AEE signals.

Figures 6(a)–6(c) show the A_{AEE} and ϕ_{AEE} images for the U-shaped 100-nm-thick Ni films on the glass, GGG, and sapphire substrates at $f = 25$ Hz and $J_c = 40$, 60, and
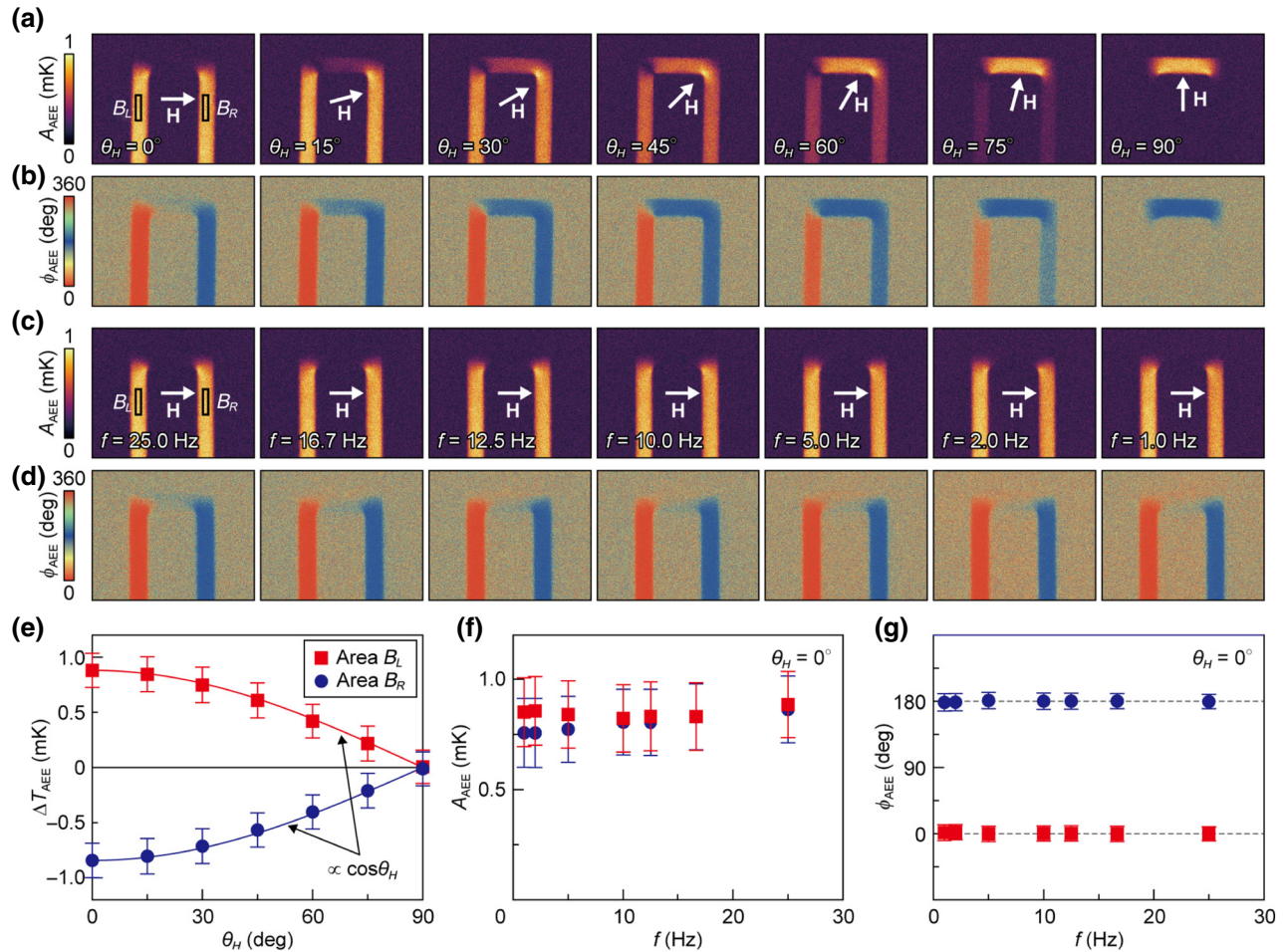

FIG. 5. (a),(b) A_{AEE} and ϕ_{AEE} images for the U-shaped 100-nm-thick Ni film on the sapphire substrate for various values of θ_H, measured at $J_c = 75$ mA and $f = 25$ Hz. (c),(d) A_{AEE} and ϕ_{AEE} images for the U-shaped 100-nm-thick Ni film on the sapphire substrate for various values of f, measured at $\theta_H = 0°$ and $J_c = 75$ mA. (e) θ_H dependence of ΔT_{AEE} on the area $B_{L/R}$ for the U-shaped 100-nm-thick Ni film on the sapphire substrate at $J_c = 75$ mA and $f = 25$ Hz. The solid curves show the $\cos\theta_H$ functions for comparison with the experimental results. (f),(g) f dependence of A_{AEE} and ϕ_{AEE} on $B_{L/R}$ for the U-shaped 100-nm-thick Ni film on the sapphire substrate, measured at $\theta_H = 0°$ and $J_c = 75$ mA. The data points in (e)–(g) are obtained by our averaging the A_{AEE} and ϕ_{AEE} values on $B_{L/R}$ defined by the squares in (a),(c). The error bars represent the standard deviation of the data in the corresponding squares.
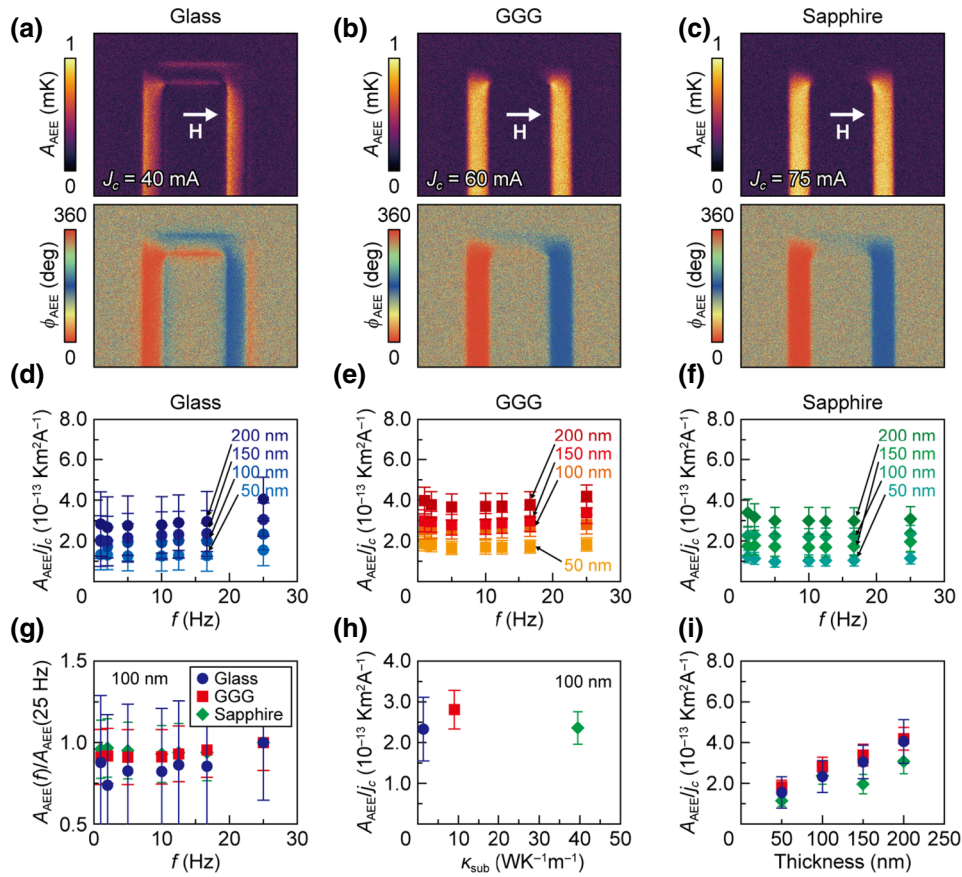
FIG. 6. (a)–(c) A_{AEE} and ϕ_{AEE} images for the U-shaped 100-nm-thick Ni film on the glass, GGG, and sapphire substrates, measured at $f = 25$ Hz and $J_c = 40$, 60, and 75 mA, respectively. (d)–(f) f dependence of A_{AEE}/j_c on B_L for the Ni films with various thicknesses on the glass, GGG, and sapphire substrates. (g) f dependence of $A_{\mathrm{AEE}}(f)/A_{\mathrm{AEE}}(25$ Hz) for the U-shaped 100-nm-thick Ni film on the glass, GGG, and sapphire substrates. (h) κ_{sub} dependence of A_{AEE}/j_c on B_L for the 100-nm-thick Ni films on the glass, GGG, and sapphire substrates at $f = 25$ Hz. (i) Ni-film thickness dependence of A_{AEE}/j_c on B_L for the Ni films on the glass, GGG, and sapphire substrates at $f = 25$ Hz. The error bars represent the standard deviation of the data in the corresponding squares. All the data shown are measured at $\theta_H = 0°$.

75 mA, respectively. The AEE signals have the same sign and similar magnitude in all the samples. As shown in Figs. 6(d)–6(g), for all the substrates, the AEE-induced temperature modulation is almost independent of f. Significantly, our results clearly show that the κ_{sub} dependence of A_{AEE}/j_c for the Ni films is much weaker than that of the AMPE signals [compare Fig. 6(h) with Fig. 4(h)], indicating that the AEE-induced temperature modulation in the IM configuration is not affected by the thermal properties of the substrates [50]. This is unlike the AMPE-induced temperature modulation, where the AMPE signal decreases with the increase in κ_{sub}, confirming the different symmetry of the AMPE and AEE. As further discussed in Sec. III D, the observed behaviors can be reproduced by taking the difference in heat-source and heat-sink distributions induced by these phenomena into account. It should also be noted that in Refs. [39,42] the AEE-induced temperature modulation in the perpendicularly magnetized (PM) configuration, where the heat current is generated

along the in-plane direction, was shown to be strongly affected by the heat loss to the substrate, which is different from the behavior for the AEE in the IM configuration. Therefore, the AEE signals in the PM configuration are expected to increase with decreasing κ_{sub} in a similar manner to the κ_{sub} dependence of the AMPE signals. Although the Ni films on the glass substrate with low κ_{sub} exhibit the clear IM-AEE features, the signals are contaminated by the PM-AEE contribution due to the small but finite perpendicular component of **M**, or nonuniformity of **H** [Fig. 6(a)]. In contrast, the pure IM-AEE signals are observed in the Ni films on the GGG and sapphire substrates having relatively high κ_{sub} [Figs. 6(b) and 6(c)], where the parasitic PM-AEE signals are suppressed.

Figure 6(i) shows that the AEE signals also increase linearly with increasing film thickness for all the substrates. This thickness dependence of the AEE signals is consistent with the results in Ref. [43] and is explained simply by the facts that the out-of-plane heat current induced by

the AEE is constant in the Ni films and that the resultant temperature difference is proportional to the integral of the heat current over the Ni thickness.

D. Numerical calculations

To confirm the observed dependences of the AMPE and AEE signals in the Ni films on the film thickness and κ_{sub}, we calculate the AMPE- and AEE-induced temperature distributions by using a finite-element method [51]. The temperature modulation due to the AMPE and AEE are evaluated in the corresponding two-dimensional cross sections (z-x plane) of the U-shaped strip by disregarding the y direction [Figs. 7(a) and 7(b)]. The model used for the calculations of the AMPE-induced (AEE-induced) temperature modulation consists of a Ni film with a width of 1.0 mm (two separated Ni films with a width of 0.2 mm) and a thickness of 50, 100, 150, or 200 nm, a substrate with a width of 10 mm and a thickness of 0.5 mm, and a black-ink layer with a width of 10 mm and a thickness of 10 μm, which corresponds to the cross section of the sample used for the experiments across $C_{L/R}$ ($B_{L/R}$) [compare Figs. 7(a) and 7(b) with Fig. 1(b) and note that the two separated Ni films in the model used for the AEE calculations represent the two leg parts of the U-shaped Ni film]. Since the LIT experiments are performed in the frequency domain, we numerically solve the heat equation in the form of

$$Ae^{-i\phi} = \frac{1}{2\pi if C\rho}[\nabla(\kappa \nabla Ae^{-i\phi}) + Q(r)], \quad (3)$$

where C, ρ, κ, and $Q(r)$ denote the specific heat, density, thermal conductivity, and heat sources. As schematically depicted in Figs. 7(a) and 7(b), $Q(r)$ is approximately set on the basis of previous calculations [39,41]. Here the AMPE generates a single heat source $+Q$ or heat sink $-Q$ around the corners of the U-shaped Ni film, where the lateral heat current is discontinuous due to the anisotropy of the Peltier coefficient [Fig. 7(a)]. In contrast, the AEE generates a heat current along the z direction; this situation is represented by the model in which the symmetric pairs of $+Q$ and $-Q$ (dipolar heat sources) are put at the top/bottom surfaces of the Ni films because the vertical heat current is discontinuous at the top/bottom surfaces [Fig. 7(b)]. The boundary conditions are $(-\kappa\nabla A)\mathbf{n} = \alpha_{air}A$ for both model boundaries, where $\mathbf{n}$ is the surface normal vector directed to the outside and $\alpha_{air} = 10$ W K^{-1} m^{-2} [41] is the heat loss to the air, except for the bottom of the substrate connected to the heat bath, at which $A = 0$ is assumed. The material parameters used for the calculations are listed in Table I. For the calculations, we assume $C\rho = 1.0 \times 10^6$ J K^{-1} m^{-3} and $\kappa = 0.5$ W K^{-1} m^{-1} for the black-ink layer (note that in Ref. [39], a similar numerical calculation using these values reproduces well the experimental results of the AEE). In the numerical calculations, the interfacial thermal resistance between the Ni films and substrates is ignored

because its contribution is much smaller than the thermal resistance of the submillimeter-thick substrate [52–54].
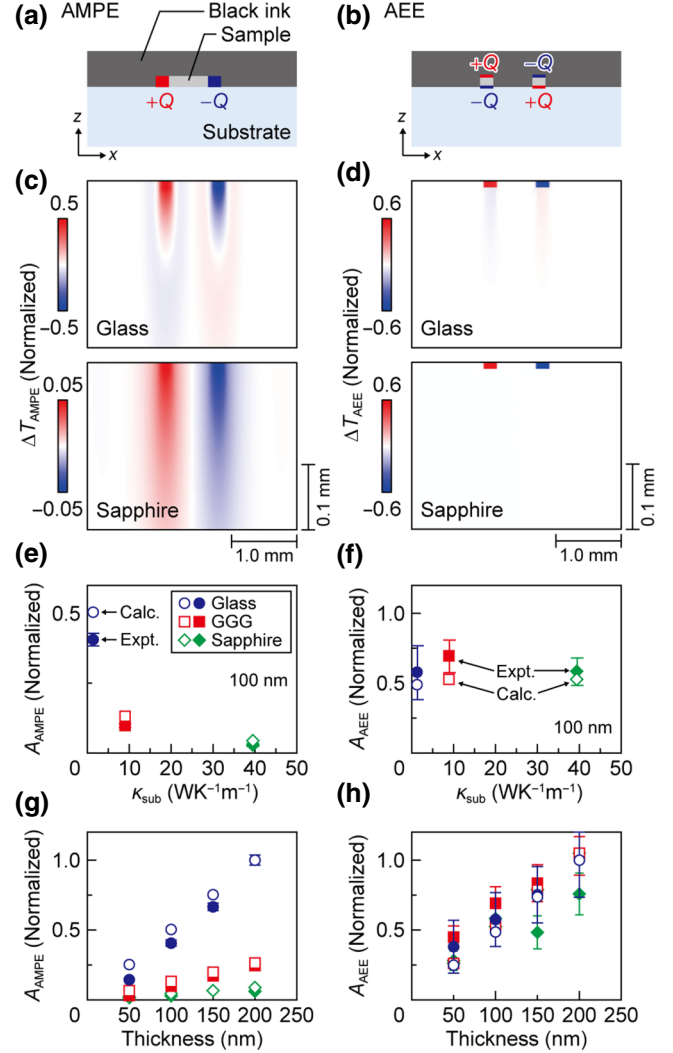

FIG. 7. (a),(b) The model structure and the location of the heat sources for the AMPE and AEE, used for the finite-element calculations. (c) Calculated ΔT_{AMPE} (equal to $A_{AMPE}\cos\phi_{AMPE}$) distributions in the z-x plane of the 100-nm-thick Ni film on the glass and sapphire substrates at $f = 25$ Hz. (d) Calculated ΔT_{AEE} (equal to $A_{AEE}\cos\phi_{AEE}$) distributions in the z-x plane of the 100-nm-thick Ni film on the glass and sapphire substrates at $f = 25$ Hz. The images in (c),(d) show the ΔT_{AMPE} and ΔT_{AEE} distributions near the top center of the black-ink/Ni-film/substrate model, where the heat sources are located near the top of the images. The ΔT_{AMPE} and ΔT_{AEE} images are magnified 10 times in the z direction. (e),(f) κ_{sub} dependence of the calculated and experimental values of A_{AMPE} and A_{AEE} for the 100-nm-thick Ni films on the glass, GGG, and sapphire substrates at $f = 25$ Hz. (g),(h) Ni-film-thickness dependence of the calculated and experimental values of A_{AMPE} and A_{AEE} for the Ni films on the glass, GGG, and sapphire substrates at $f = 25$ Hz. The calculated and experimental data in (e)–(h) are normalized by the A_{AMPE} or A_{AEE} values for the 200-nm-thick Ni film on the glass substrate.

To understand the behavior of the AMPE in thin films on substrates, we calculate the temperature distribution in the model shown in Fig. 7(a), where the width of the heat source and heat sink is set to be 0.2 mm. Calculated ΔT_{AMPE} (equal to $A_{\mathrm{AMPE}}\cos\phi_{\mathrm{AMPE}}$) images show remarkable broadening of the AMPE-induced temperature modulation in the substrates. Importantly, the resultant temperature distribution is strongly dependent on the thermal properties of the substrate; as shown in Fig. 7(c), the magnitude of the calculated AMPE-induced temperature modulation for the sapphire substrate is much smaller than that for the glass substrate. In Fig. 7(e), we plot the calculated values of A_{AMPE} on the top surface of the black ink around the center of the positive heat source as a function of κ_{sub}, showing that the magnitude of A_{AMPE} decreases with increasing κ_{sub} and the behavior is consistent with the experimental results. The relationship between the Ni-film thickness and the AMPE-induced temperature modulation is also reproduced by the numerical calculations for all the substrates [Fig. 7(g)].

Next we show the calculated temperature distribution induced by the AEE. In the model shown in Fig. 7(b), the thickness of the heat sources and heat sinks is set to be 1% of the film thickness and the width is the same as that of the Ni films (0.2 mm). The polarity of the dipolar heat sources is reversed between the left and right Ni films according to the symmetry of the AEE in our experiments [compare Fig. 7(b) with Fig. 1(a)]. The calculated temperature distributions show that the AEE-induced temperature modulation appears only in the vicinity of the Ni films and that the magnitude of the temperature modulation on the top surface of the sample is much greater than that inside the substrate, a situation that is similar to the temperature distribution induced by the spin Peltier effect [38]. Owing to this temperature distribution, the temperature modulation induced by the AEE in the IM configuration is hardly affected by the thermal properties of the substrates. In fact, as shown in Figs. 7(d) and 7(f), the magnitude of the calculated A_{AEE} values on the surface of the black ink is almost independent of the substrate species, consistent with the experimental results (note that the small decrease in the AEE-induced temperature modulation for the glass sample is because the heat loss to the substrate through the lateral edges of the Ni layer is not negligibly small as a result of comparable thermal conductivity between glass and the black-ink layer [55]). The relationship between the Ni-film thickness and the AEE-induced temperature modulation, demonstrated experimentally, is also reproduced by the numerical calculations for all the substrates [Fig. 7(h)].

IV. SUMMARY

We investigate the AMPE and AEE in polycrystalline Ni thin films of differing thickness (50, 100, 150, and 200 nm) deposited on glass, GGG, and sapphire substrates by using the LIT technique. We demonstrate a procedure to extract the pure AMPE- and AEE-induced temperature-modulation contributions by separating them from each other and from the background due to the conventional Peltier effect. Our results show that the Ni films exhibit clear current-induced temperature modulation showing $\cos 2\theta_H$ ($\cos\theta_H$) symmetry, confirming the presence of the AMPE (AEE) signals. Both the AMPE-induced temperature modulation and the AEE-induced temperature modulation increase linearly with increase in the film thickness and the AMPE-induced temperature modulation increases with decreasing frequency of the charge current applied to the Ni films, whereas the AEE-induced temperature modulation is almost independent of the frequency. The AMPE-induced temperature modulation decreases with increasing thermal conductivity of the substrates due to the heat loss from the films to the substrates, whereas the AEE-induced temperature modulation is almost independent of the thermal conductivity, behaviors that are reproduced by the numerical calculations based on a two-dimensional finite-element method. These results establish the importance of the sample dimensions and substrate thermal properties in determining the behaviors of the AMPE and AEE in thin films, highlighting the different symmetry of the two effects. Importantly, the behaviors of the AMPE and AEE revealed by this study are not limited to LIT experiments; the substrate and thickness dependences of the temperature modulation induced by these phenomena have to be taken into account irrespective of the measurement technique.

[1] N. W. Ashcroft and N. D. Mermin, *Solid State Physics* (Saunders College, Philadelphia, 1976).
[2] D. Kondepudi and I. Prigogine, *Modern Thermodynamics: From Heat Engines to Dissipative Structures* (Wiley, Chichester, 1998).
[3] R. M. Bozorth, Magnetoresistance and domain theory of iron-nickel alloys, Phys. Rev. **70,** 923 (1946).
[4] R. Karplus and J. M. Luttinger, Hall effect in ferromagnetics, Phys. Rev. **95,** 1154 (1954).

[5] J. P. Jan, in *Solid State Physics*, edited by F. Seitz and D. Turnbull (Academic, New York, 1957), Vol. 5, pp. 1–96.

[6] T. McGuire and R. Potter, Anisotropic magnetoresistance in ferromagnetic 3*d* alloys, IEEE Trans. Magn. **11**, 1018 (1975).

[7] G. N. Grannemann and L. Berger, Magnon-drag Peltier effect in a Ni-Cu alloy, Phys. Rev. B **13**, 2072 (1976).

[8] M. Johnson and R. H. Silsbee, Thermodynamic analysis of interfacial transport and of the thermomagnetoelectric system, Phys. Rev. B **35**, 4959 (1987).

[9] Y. Wang, Z. A. Xu, T. Kakeshita, S. Uchida, S. Ono, Y. Ando, and N. P. Ong, Onset of the vortexlike Nernst signal above T_c in $La_{2-x}Sr_xCuO_4$ and $Bi_2Sr_{2-y}La_yCuO_6$, Phys. Rev. B **64**, 224519 (2001).

[10] W.-L. Lee, S. Watauchi, V. L. Miller, R. J. Cava, and N. P. Ong, Anomalous Hall Heat Current and Nernst Effect in the $CuCr_2Se_{4-x}Br_x$ Ferromagnet, Phys. Rev. Lett. **93**, 226601 (2004).

[11] D. Xiao, Y. Yao, Z. Fang, and Q. Niu, Berry-Phase Effect in Anomalous Thermoelectric Transport, Phys. Rev. Lett. **97**, 026603 (2006).

[12] J.-E. Wegrowe, Q. A. Nguyen, M. Al-Barki, J.-F. Dayen, T. L. Wade, and H.-J. Drouhin, Anisotropic magnetothermopower: Contribution of interband relaxation, Phys. Rev. B **73**, 134422 (2006).

[13] Y. Pu, D. Chiba, F. Matsukura, H. Ohno, and J. Shi, Mott Relation for Anomalous Hall and Nernst Effects in $Ga_{1-x}Mn_xAs$ Ferromagnetic Semiconductors, Phys. Rev. Lett. **101**, 117208 (2008).

[14] K. Uchida, S. Takahashi, K. Harii, J. Ieda, W. Koshibae, K. Ando, S. Maekawa, and E. Saitoh, Observation of the spin Seebeck effect, Nature **455**, 778 (2008).

[15] K. Uchida, J. Xiao, H. Adachi, J. Ohe, S. Takahashi, J. Ieda, T. Ota, Y. Kajiwara, H. Umezawa, H. Kawai, G. E. W. Bauer, S. Maekawa, and E. Saitoh, Spin Seebeck insulator, Nat. Mater. **9**, 894 (2010).

[16] C. M. Jaworski, J. Yang, S. Mack, D. D. Awschalom, J. P. Heremans, and R. C. Myers, Observation of the spin-Seebeck effect in a ferromagnetic semiconductor, Nat. Mater. **9**, 898 (2010).

[17] K. Uchida, H. Adachi, T. Ota, H. Nakayama, S. Maekawa, and E. Saitoh, Observation of longitudinal spin-Seebeck effect in magnetic insulators, Appl. Phys. Lett. **97**, 172505 (2010).

[18] M. Walter, J. Walowski, V. Zbarsky, M. Munzenberg, M. Schafers, D. Ebke, G. Reiss, A. Thomas, P. Peretzki, M. Seibt, J. S. Moodera, M. Czerner, M. Bachmann, and C. Heiliger, Seebeck effect in magnetic tunnel junctions, Nat. Mater. **10**, 742 (2011).

[19] N. Liebing, S. Serrano-Guisan, K. Rott, G. Reiss, J. Langer, B. Ocker, and H. W. Schumacher, Tunneling Magnetothermopower in Magnetic Tunnel Junction Nanopillars, Phys. Rev. Lett. **107**, 177201 (2011).

[20] T. Naydenova, P. Durrenfeld, K. Tavakoli, N. Pégard, L. Ebel, K. Pappert, K. Brunner, C. Gould, and L. W. Molenkamp, Diffusion Thermopower of (Ga, Mn)As/GaAs Tunnel Junctions, Phys. Rev. Lett. **107**, 197201 (2011).

[21] S. Y. Huang, W. G. Wang, S. F. Lee, J. Kwo, and C. L. Chien, Intrinsic Spin-Dependent Thermal Transport, Phys. Rev. Lett. **107**, 216604 (2011).

[22] A. D. Avery, R. Sultan, D. Basset, D. Wei, and B. L. Zink, Thermopower and resistivity in ferromagnetic thin films near room temperature, Phys. Rev. B **83**, 100401(R) (2011).

[23] M. Czerner, M. Bachmann, and C. Heiliger, Spin caloritronics in magnetic tunnel junctions: Ab initio studies, Phys. Rev. B **83**, 132405 (2011).

[24] G. E. W. Bauer, E. Saitoh, and B. J. van Wees, Spin caloritronics, Nat. Mater. **11**, 391 (2012).

[25] S. Y. Huang, X. Fan, D. Qu, Y. P. Chen, W. G. Wang, J. Wu, T. Y. Chen, J. Q. Xiao, and C. L. Chien, Transport Magnetic Proximity Effects in Platinum, Phys. Rev. Lett. **109**, 107204 (2012).

[26] A. D. Avery, M. R. Pufall, and B. L. Zink, Observation of the Planar Nernst Effect in Permalloy and Nickel Thin Films with In-Plane Thermal Gradients, Phys. Rev. Lett. **109**, 196602 (2012).

[27] A. D. Avery, M. R. Pufall, and B. L. Zink, Determining the planar Nernst effect from magnetic-field-dependent thermopower and resistance in nickel and permalloy thin films, Phys. Rev. B **86**, 184408 (2012).

[28] R. Mitdank, M. Handwerg, C. Steinweg, W. Tollner, M. Daub, K. Nielsch, and S. F. Fischer, Enhanced magnetothermoelectric power factor of a 70 nm Ni-nanowire, J. Appl. Phys. **111**, 104320 (2012).

[29] M. Schmid, S. Srichandan, D. Meier, T. Kuschel, J.-M. Schmalhorst, M. Vogel, G. Reiss, C. Strunk, and C. H. Back, Transverse Spin Seebeck Effect Versus Anomalous and Planar Nernst Effects in Permalloy Thin Films, Phys. Rev. Lett. **111**, 187201 (2013).

[30] D. Meier, D. Reinhardt, M. Schmid, C. H. Back, J.-M. Schmalhorst, T. Kuschel, and G. Reiss, Influence of heat flow directions on Nernst effects in Py/Pt bilayers, Phys. Rev. B **88**, 184425 (2013).

[31] C. Heiliger, C. Franz, and M. Czerner, Ab initio studies of the tunneling magneto-Seebeck effect: Influence of magnetic material, Phys. Rev. B **87**, 224412 (2013).

[32] S. R. Boona, R. C. Myers, and J. P. Heremans, Spin caloritronics, Energy Environ. Sci. **7**, 885 (2014).

[33] J. Flipse, F. K. Dejene, D. Wagenaar, G. E. W. Bauer, J. B. Youssef, and B. J. van Wees, Observation of the Spin Peltier Effect for Magnetic Insulators, Phys. Rev. Lett. **113**, 027601 (2014).

[34] V. P. Amin, J. Zemen, J. Železný, T. Jungwirth, and J. Sinova, Large-tunneling anisotropic magneto-Seebeck effect in a CoPt/MgO/Pt tunnel junction, Phys. Rev. B **90**, 140406(R) (2014).

[35] D. Meier, D. Reinhardt, M. van Straaten, C. Klewe, M. Althammer, M. Schreier, S. T. B. Goennenwein, A. Gupta, M. Schmid, C. H. Back, J.-M. Schmalhorst, T. Kuschel, and Günter Reiss, Longitudinal spin Seebeck effect contribution in transverse spin Seebeck effect experiments in Pt/YIG and Pt/NFO, Nat. Commun. **6**, 8211 (2015).

[36] J. Shan, F. K. Dejene, J. C. Leutenantsmeyer, J. Flipse, M. Munzenberg, and B. J. van Wees, Comparison of the magneto-Peltier and magneto-Seebeck effect in magnetic tunnel junctions, Phys. Rev. B **92**, 020414(R) (2015).

[37] K. S. Das, F. K. Dejene, B. J. van Wees, and I. J. Vera-Marun, Anisotropic Hanle line shape via magnetothermoelectric phenomena, Phys. Rev. B **94**, 180403(R) (2016).

[38] S. Daimon, R. Iguchi, T. Hioki, E. Saitoh, and K. Uchida, Thermal imaging of spin Peltier effect, Nat. Commun. **7,** 13754 (2016).

[39] T. Seki, R. Iguchi, K. Takanashi, and K. Uchida, Visualization of anomalous Ettingshausen effect in a ferromagnetic film: Direct evidence of different symmetry from spin Peltier effect, Appl. Phys. Lett. **112,** 152403 (2018).

[40] A. Yagmur, R. Iguchi, S. Geprägs, A. Erb, S. Daimon, E. Saitoh, R. Gross, and K. Uchida, Lock-in thermography measurements of the spin Peltier effect in a compensated ferrimagnet and its comparison to the spin Seebeck effect, J. Phys. D: Appl. Phys. **51,** 194002 (2018).

[41] K. Uchida, S. Daimon, R. Iguchi, and E. Saitoh, Observation of anisotropic magneto-Peltier effect in nickel, Nature **588,** 95 (2018).

[42] T. Seki, R. Iguchi, K. Takanashi, and K. Uchida, Relationship between anomalous Ettingshausen effect and anomalous Nernst effect in an FePt thin film, J. Phys. D: Appl. Phys. **51,** 254001 (2018).

[43] R. Iguchi, A. Yagmur, Y.-C. Lau, S. Daimon, E. Saitoh, M. Hayashi, and K. Uchida, Thermographic measurements of spin-current-induced temperature modulation in metallic bilayers, Phys. Rev. B **98,** 014402 (2018).

[44] K. Uchida, M. Sasaki, Y. Sakuraba, R. Iguchi, S. Daimon, E. Saitoh, and M. Goto, Combinatorial investigation of spin-orbit materials using spin Peltier effect, Sci. Rep. **8,** 16067 (2018).

[45] K. Masuda, K. Uchida, R. Iguchi, and Y. Miura, First-principles study of anisotropic magneto-Peltier effect, Phys. Rev. B **99,** 104406 (2019).

[46] T. Kuschel, M. Czerner, J. Walowski, A. Thomas, H. W. Schumacher, G. Reiss, C. Heiliger, and M. Münzenberget, Tunnel magneto-Seebeck effect, J. Phys. D: Appl. Phys. **52,** 133001 (2019).

[47] H. Straube, J.-M. Wagner, and O. Breitenstein, Measurement of the Peltier coefficient of semiconductors by lock-in thermography, Appl. Phys. Lett. **95,** 052107 (2009).

[48] O. Breitenstein, W. Warta, and M. Langenkamp, *Lock-in Thermography: Basics and Use for Evaluating Electronic Devices and Materials* (Springer, Berlin and Heidelberg, 2010).

[49] O. Wid, J. Bauer, A. Muller, O. Breitenstein, S. S. P. Parkin, and G. Schmidt, Investigation of the unidirectional spin heat conveyer effect in a 200 nm thin yttrium iron garnet film, Sci. Rep. **6,** 28233 (2016).

[50] The average temperature of the Ni films is affected by κ_{sub}; when the same charge-current density is applied to the films, the temperature increase due to Joule heating becomes larger when κ_{sub} is smaller, because the bottom

[51] F. Hecht, New development in freefem++, J. Numer. Math. **20,** 251 (2012).

[52] H.-C. Chien, D.-J. Yao, and C.-T. Hsu, Measurement and evaluation of the interfacial thermal resistance between a metal and a dielectric, Appl. Phys. Lett. **93,** 231910 (2008).

[53] R. M. Costescu, M. A. Wall, and D. G. Cahill, Thermal conductance of epitaxial interfaces, Phys. Rev. B **67,** 054302 (2003).

[54] R. J. Stevens, A. N. Smith, and P. M. Norris, Measurement of thermal boundary conductance of a series of metal-dielectric interfaces by the transient thermoreflectance technique, J. Heat Transfer. **127,** 315 (2005).

[55] The small κ_{sub} dependence of the AEE-induced temperature modulation can be explained as follows. First, it is important to note that when κ_{sub} is large, the substrate works as a heat bath and the temperature of the Ni/substrate interface is fixed. In this condition, the vertical heat current induced by the AEE efficiently changes the temperature at the top surface of the sample. However, the AEE decreases the resultant temperature modulation at the surface when the thermal connection to the substrate through the lateral edges of the Ni layer is not negligibly small. This situation happens when κ_{sub} is small. When the contribution of the heat flow from the lateral edges to the substrate bottom through the black-ink layer increases, the temperature at the Ni/substrate interface is no longer maintained. As a result, the surface temperature modulation decreases and opposite temperature modulation appears at the bottom of the Ni layer, resulting in the small temperature change near the substrate in Fig. 7(d). We also note that this substrate dependence decreases when the width of the Ni layer increases and disappears when the black-ink layer (or thermal conductor surrounding the Ni layer) is absent.

[56] G. A. Slack, Thermal conductivity of MgO, Al$_2$O$_3$, MgAl$_2$O$_4$, and Fe$_3$O$_4$ crystals from 3° to 300°K, Phys. Rev. **126,** 427 (1962).

[57] G. A. Slack and D. W. Oliver, Thermal conductivity of garnets and phonon scattering by rare-earth ions, Phys. Rev. B **4,** 592 (1971).

[58] A. D. Avery, S. J. Mason, D. Bassett, D. Wesenberg, and B. L. Zink, Thermal and electrical conductivity of approximately 100-nm permalloy, Ni, Co, Al, and Cu films and examination of the Wiedemann-Franz Law, Phys. Rev. B **92,** 214410 (2015).

of the substrate is attached to the heat bath. Although the increase of the average temperature does not appear in the lock-in thermal images, substrates with higher κ_{sub} allow us to increase the charge-current density while keeping the sample temperature as constant as possible.